

# Sum frequency generation from real-time simulations in two-dimensional crystals

Mike N. Pionteck<sup>1\*</sup>, Myrta Grüning<sup>2,3</sup>, Simone Sanna<sup>1</sup>, Claudio Attaccalite<sup>3,4</sup>

**1** Institut für Theoretische Physik and Center for Materials Research (LaMa),  
Justus-Liebig-Universität Gießen, 35392 Gießen, Germany

**2** School of Mathematics and Physics, Queen's University Belfast, Belfast BT7 1NN,  
United Kingdom

**3** European Theoretical Spectroscopy Facilities (ETSF)

**4** CNRS/Aix-Marseille Université, Centre Interdisciplinaire de Nanoscience de Marseille  
UMR 7325 Campus de Luminy, 13288 Marseille cedex 9, France

\* Mike.Pionteck@theo.physik.uni-giessen.de

## Abstract

Sum frequency generation (SFG) and difference frequency generation (DFG) are second order nonlinear processes where two lasers with frequencies  $\omega_1$  and  $\omega_2$  combine to produce a response at frequency  $\omega = \omega_1 \pm \omega_2$ . Compared with other nonlinear responses such as second-harmonic generation, SFG and DFG allow for tunability over a larger range. Moreover, the optical response can be enhanced by selecting the two laser frequencies in order to match specific electron-hole transitions.

Here, we propose a first-principles framework based on the real-time solution of an effective Schrödinger equation to calculate the SFG and DFG in various systems, such as bulk materials, 2D materials, and molecules. Within this framework, one can select from various levels of theory for the effective one-particle Hamiltonian to account for local-field effects and electron-hole interactions. To assess the approach, we calculate the SFG and DFG of two-dimensional crystals, *h*-BN and MoS<sub>2</sub> monolayers, both within the independent-particle picture and including many-body effects. Additionally, we demonstrate that our approach can also extract higher-order response functions, such as field-induced second-harmonic generation. We provide an example using bilayer *h*-BN.

---

## Contents

<b>1</b>	<b>Introduction</b>	<b>2</b>
<b>2</b>	<b>Theoretical background</b>	<b>3</b>
2.1	Nonlinear response from real-time simulations	3
2.2	Sum/Difference frequency generation	4
2.3	Field-Induced Second-Harmonic Generation	5
<b>3</b>	<b>Signal processing: nonlinear susceptibilities</b>	<b>5</b>
3.1	One external monochromatic field	6
3.2	Two external monochromatic fields	6
3.2.1	Further numerical considerations	8
<b>4</b>	<b>Computational Details</b>	<b>10</b>
<b>5</b>	<b>Results</b>	<b>10</b>
5.1	SFG and DFG in monolayer <i>h</i> -BN	11
5.2	SFG and DFG in monolayer MoS <sub>2</sub>	13

5.3	Field-Induced Second-Harmonic Generation	13
<b>6</b>	<b>Conclusions</b>	<b>14</b>
	<b>References</b>	<b>15</b>

---

## 1 Introduction

Sum frequency generation (SFG) and difference frequency generation (DFG) spectroscopy are powerful experimental techniques where the spectrum is the second-order nonlinear optical response  $\chi^{(2)}$  resulting from the combination of two laser fields (see Fig. 1(a) and (b)). These techniques are highly sensitive to surfaces and interfaces [1–3]. In recent years, there has been a growing interest in the application of SFG/DFG in condensed matter physics. In particular, SFG/DFG was reported in layered MoS<sub>2</sub> and related heterosystems using either band-filtered supercontinuum illumination [4,5] or wavelength-dependent spectroscopy [5–7]. More interestingly, one can make the SFG dual resonant with the exciton, strongly enhancing its response function, as shown recently in two-dimensional (2D) materials [8]. Then, SFG can serve to explore exciton-exciton transitions as an alternative and complementary technique to pump and probe spectroscopy [9]. The design and interpretation of such experiments call for the development of theoretical approaches that can, for a specific material, capture both the nonlinear light-matter interaction and the many-body physics of excitons.

So far, few theoretical studies have been reported in the literature on SFG and DFG in solids. The SFG was investigated using either simple two-band models [10] or from first-principles, using the Greenwood-Kubo formalism, within an independent-particle picture [8]—thus missing excitonic effects. In this work, we put forward a general approach to extract the SFG and DFG spectra from real-time simulations. We implement this approach within the first-principles framework of Ref. [11] in which the coupling of the electrons with the external electric field based on the Berry-phase formulation of the dynamical polarization [12] and many-body effects, including excitonic effects, are accounted for through an effective Hamiltonian [13]. We apply the approach to calculate the SFG and DFG of MoS<sub>2</sub> and *h*-BN monolayers, both within the independent-particle picture and including excitonic effects. The approach presented is not limited to the SFG and DFG but allows an efficient calculation of other response functions, such as field-induced second-harmonic generation (FI-SHG) [14,15]. FI-SHG involves applying an electric field, such as laser pulses, DC current, or an intense terahertz (THz) electric field, to a crystal and measuring the resulting second-harmonic intensity, which can provide important insights into the material properties. Centrosymmetric crystals, which have a null second harmonic response (in the dipole approximation), are of particular interest because the applied field breaks the symmetry and produces even-order harmonic radiation. For a static electric field a real-time approach to study FI-SHG has been proposed in Ref. [16]. Here we go a step further, and put forward a framework to simulate FI-SHG in presence of time-dependent pump fields. For a *h*-BN bilayer, which is a centrosymmetric crystal, we calculate the second harmonic response induced by a THz field breaking the inversion symmetry [Fig. 1(c)].

The manuscript is organized as follows. In Sec. 2, we present the real-time approach used to obtain the dynamical polarization (Sec. 2.1) and provide a description of SFG,

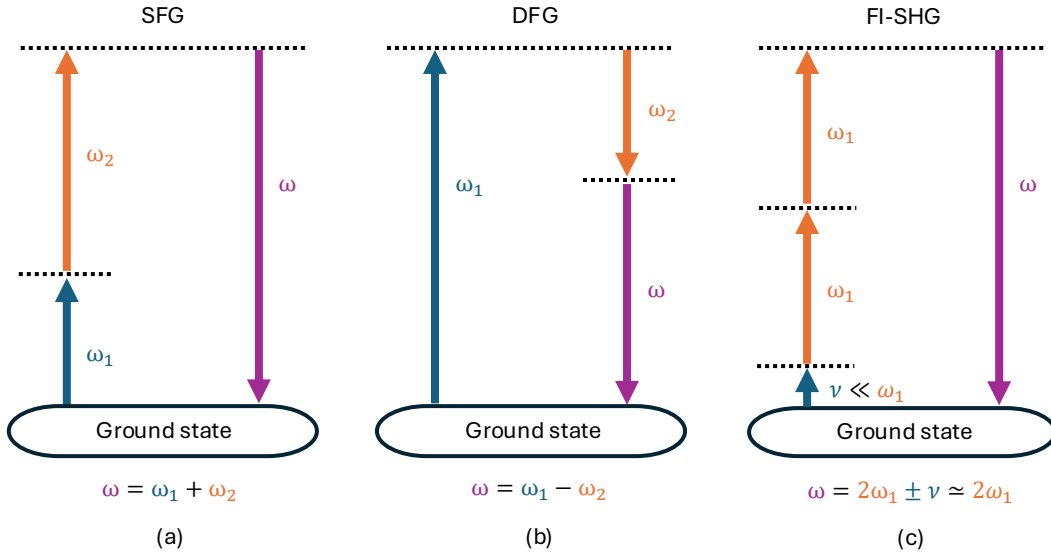


Figure 1: A schematic representation of the nonlinear processes studied in this work: (a) sum frequency generation (SFG), (b) difference frequency generation (DFG) and (c) field-induced second-harmonic generation (FI-SHG).

DFG, and FI-SHG through their Lehmann representations (Secs. 2.2-2.3). In Sec. 3, we detail and contrast the signal process techniques (discrete Fourier analysis and nonlinear least squares optimization) used to obtain the SFG/DFG and FI-SHG. After outlining the computational details in Sec. 4, we discuss in Sec. 5 the results obtained for the SFG and DFG of MoS<sub>2</sub> and *h*-BN monolayers and for the FI-SHG in the *h*-BN bilayer.

## 2 Theoretical background

We obtain the nonlinear optical susceptibilities from the time evolution of Bloch electrons in a uniform time-dependent electric field [11]. We extend the approach developed in Ref. [11] that was limited to a single monochromatic field in Sec. 2.1. This extension allows us to access a range of nonlinear phenomena. We focus on the SFG and DFG (Sec. 2.2) and the FI-SHG (Sec. 2.3).

### 2.1 Nonlinear response from real-time simulations

The time evolution of the electronic system induced by two monochromatic homogeneous fields  $\mathcal{E}_1(t)$  and  $\mathcal{E}_2(t)$  is described by the following equation of motions (EOMs) for the valence Bloch states:

$$i\hbar \frac{d}{dt} |v_{m\mathbf{k}}\rangle = \left\{ H_{\mathbf{k}}^{\text{MB}} + ie [\mathcal{E}_1(t) + \mathcal{E}_2(t)] \cdot \tilde{\partial}_{\mathbf{k}} \right\} |v_{m\mathbf{k}}\rangle, \quad (1)$$

where  $|v_{m\mathbf{k}}\rangle = |v_{m\mathbf{k}}(t)\rangle$  is the periodic part of the time-dependent Bloch states. On the right-hand side of Eq. (1), the second term describes the coupling with the external field in the dipole approximation. The coupling takes the form of a  $\mathbf{k}$ -derivative operator. The tilde indicates that the operator is gauge covariant, i.e. the solutions of Eq. (1) do not change under unitary rotation at  $\mathbf{k}$  (see Ref. [12] for more details).  $H_{\mathbf{k}}^{\text{MB}}$  is the effective many-body Hamiltonian. Different correlation effects can be accounted for by constructing the corresponding effective Hamiltonian. The most accurate effective Hamiltonian we

consider in this work is the time-dependent adiabatic GW (TD-aGW) [17] approximation which accounts for electron-hole interaction and local field effects:

$$H_{\mathbf{k}}^{\text{MB}} \equiv H_{\mathbf{k}}^{\text{KS}} + \Delta H_{\mathbf{k}} + V_h(\mathbf{r})[\Delta\rho] + \Sigma_{\text{SEX}}[\Delta\gamma], \quad (2)$$

where  $H_{\mathbf{k}}^{\text{KS}}$  is the Hamiltonian of the unperturbed (zero-field) Kohn-Sham system [18],  $\Delta H_{\mathbf{k}}$  is the scissors operator applied to the Kohn-Sham eigenvalues, and the term  $V_h(\mathbf{r})[\Delta\rho]$  is the real-time Hartree potential [11], responsible for the local field effects [19] arising from system inhomogeneities. The term  $\Sigma_{\text{SEX}}$  is the screened-exchange self-energy that accounts for the electron-hole interaction [17].  $\Delta\rho$  and  $\Delta\gamma$  are, respectively, the variations of the density and the density matrix induced by the external fields. In the limit of small perturbation Eqs. (1) and (2) reproduce the optical absorption calculated with the standard  $GW + \text{BSE}$  approach, [19] as shown both analytically and numerically in Ref. [17]. The other approximation we consider is the independent particle approximation (IPA) that corresponds to  $H^{\text{MB}} \equiv H^{\text{KS}}$ .

From the solutions  $|v_{m\mathbf{k}}\rangle$  in Eq. (1), we calculate the real-time polarization along the lattice vector  $\mathbf{a}$  as [12]:

$$P_{\parallel}(t) = -\frac{ef|\mathbf{a}|}{2\pi V} \text{Im} \log \prod_{\mathbf{k}}^{N_{\mathbf{k}}-1} \det S(\mathbf{k}, \mathbf{k} + \mathbf{q}; t), \quad (3)$$

where  $S(\mathbf{k}, \mathbf{k} + \mathbf{q}; t)$  is the overlap matrix between the time-dependent valence states  $|v_{n\mathbf{k}}\rangle$  and  $|v_{m\mathbf{k}+\mathbf{q}}\rangle$ ,  $V$  is the unit cell volume,  $f$  is the spin degeneracy,  $N_{\mathbf{k}}$  is the number of  $\mathbf{k}$ -points along the polarization direction, and  $\mathbf{q} = 2\pi/(N_{\mathbf{k}}\mathbf{a})$ . Then, the  $n$ -order susceptibilities  $\chi^{(n)}$  are extracted from the frequency-dependent polarization expanded in a power series of the incident fields as:

$$P_{\alpha}(\omega) = \sum_{\beta=1}^3 \sum_{i=1}^2 \chi_{\alpha\beta}^{(1)}(\omega; \omega_i) \mathcal{E}_{\beta}(\omega_i) + \sum_{\beta,\gamma=1}^3 \sum_{i,j=1}^2 \chi_{\alpha\beta\gamma}^{(2)}(\omega; \omega_i, \omega_j) \mathcal{E}_{\beta}(\omega_i) \mathcal{E}_{\gamma}(\omega_j) + O(\mathcal{E}^3), \quad (4)$$

where  $\omega_i, \omega_j$  are frequencies of the perturbing fields  $\mathcal{E}_{\beta}, \mathcal{E}_{\gamma}$  and  $\omega$  the frequency of the outgoing polarization, with  $\alpha, \beta, \gamma$  denoting the Cartesian directions.

## 2.2 Sum/Difference frequency generation

In Fig. 1(a),(b) we present a schematic representation of the SFG and DFG response functions studied in this work that correspond to  $\chi^{(2)}(\omega, \omega_i, \omega_j)$  in Eq. (4) with  $\omega = \omega_i \pm \omega_j$ . In Sec. 3.2, we explain how the SFG and DFG are derived from the time-dependent polarization. Here, we discuss their Lehmann representation which is useful in the interpretation of the results.

The general form of the second-order susceptibility,  $\chi_{\alpha\beta\gamma}^{(2)}(\omega_3; \omega_1, \omega_2)$  in the Lehmann representation, obtained through second-order perturbation theory [20] reads:

$$\begin{aligned} \chi_{\alpha\beta\gamma}^{(2)}(\omega_3; \omega_1, \omega_2) \approx & \frac{-ie^3}{m^3 \tilde{\omega}_3 \tilde{\omega}_1 \tilde{\omega}_2} \sum_{\lambda\lambda'} \left[ \frac{\alpha_{0\lambda} \beta_{\lambda\lambda'} \gamma_{\lambda'0}}{(\tilde{\omega}_2 - \Omega_{\lambda'}) (\tilde{\omega}_3 - \Omega_{\lambda})} + \frac{\beta_{0\lambda} \gamma_{\lambda\lambda'} \alpha_{\lambda'0}}{(\tilde{\omega}_1 + \Omega_{\lambda}) (\tilde{\omega}_3 + \Omega_{\lambda'})} \right. \\ & - \frac{\gamma_{0\lambda} \alpha_{\lambda\lambda'} \beta_{\lambda'0}}{(\tilde{\omega}_1 - \Omega_{\lambda'}) (\tilde{\omega}_2 + \Omega_{\lambda})} + \frac{\alpha_{0\lambda} \gamma_{\lambda\lambda'} \beta_{\lambda'0}}{(\tilde{\omega}_1 - \Omega_{\lambda'}) (\tilde{\omega}_3 - \Omega_{\lambda})} \\ & \left. + \frac{\gamma_{0\lambda} \beta_{\lambda\lambda'} \alpha_{\lambda'0}}{(\tilde{\omega}_2 + \Omega_{\lambda}) (\tilde{\omega}_3 + \Omega_{\lambda'})} - \frac{\beta_{0\lambda} \alpha_{\lambda'} \gamma_{\lambda'0}}{(\tilde{\omega}_2 - \Omega_{\lambda'}) (\tilde{\omega}_1 + \Omega_{\lambda})} \right] \end{aligned} \quad (5)$$

where  $\Omega_{\lambda}$  are the excitation energies of the system, and  $\alpha_{\lambda'}$  refers to momentum matrix elements  $\langle \lambda | P_{\alpha} | \lambda' \rangle$  between two excited states and similarly for  $\beta_{\lambda\lambda'}$  and  $\gamma_{\lambda\lambda'}$ . Here,

$\tilde{\omega}_1 = \omega_1 + i\eta$ ,  $\tilde{\omega}_2 = \omega_2 + i\eta$  and  $\tilde{\omega}_3 = \tilde{\omega}_1 + \tilde{\omega}_2$ .  $\mathbf{P}$  is the many-body momentum operator, i.e.  $\mathbf{P} = \sum_i \mathbf{p}_i$  where  $\mathbf{p}_i$  is the single-particle momentum operator acting on particle  $i$  and  $\eta$  is a small positive number that introduces dephasing/dissipation effects. An approximation of Eq. (5) can be derived by replacing many-body states and energies with excitonic ones [19]:  $|\lambda\rangle \simeq |\Psi_\lambda^{\text{exc}}\rangle$  and  $\Omega_\lambda \simeq E_\lambda$ . When we consider the SFG case  $\omega_3 = \omega_1 + \omega_2$ , we retain only positive contributions to the  $\chi^{(2)}$  and we get

$$\chi_{\alpha\beta\gamma}^{(2)}(\omega_1 + \omega_2; \omega_1, \omega_2) \approx \sum_{\lambda\lambda'} \left[ \frac{P_{\alpha,0\lambda} P_{\beta,\lambda\lambda'} P_{\gamma,\lambda'0}}{(\tilde{\omega}_2 - E_{\lambda'}) (\tilde{\omega}_1 + \tilde{\omega}_2 - E_\lambda)} - \frac{P_{\gamma,0\lambda} P_{\alpha,\lambda\lambda'} P_{\beta,\lambda'0}}{(\tilde{\omega}_1 - E_{\lambda'}) (\tilde{\omega}_2 + E_\lambda)} \right. \\ \left. + \frac{P_{\alpha,0\lambda} P_{\gamma,\lambda\lambda'} P_{\beta,\lambda'0}}{(\tilde{\omega}_1 - E_{\lambda'}) (\tilde{\omega}_1 + \tilde{\omega}_2 - E_\lambda)} - \frac{P_{\beta,0\lambda} P_{\alpha,\lambda\lambda'} P_{\gamma,\lambda'0}}{(\tilde{\omega}_2 - E_{\lambda'}) (\tilde{\omega}_1 + E_\lambda)} \right] \quad (6)$$

where  $\lambda$  now indicates the excitonic state and  $P_{\alpha,\lambda\lambda'} = \langle \Psi_\lambda^{\text{exc}} | p_\alpha | \Psi_{\lambda'}^{\text{exc}} \rangle$  [9]. A similar procedure has been applied in the literature for the second-harmonic generation (SHG) case [21, 22]. From this formula we could expect strong peaks when  $\omega_1 + \omega_2$  is resonant with excitonic energy or when single laser frequencies  $\omega_1, \omega_2$  are resonant with an exciton. Note that the first and third terms have poles at both one-photon (e.g.  $\omega_1, \omega_2$ ) and two-photon ( $\omega_1 + \omega_2$ ) resonances. Finally, if  $P_{\alpha,\lambda\lambda'}$  is different from zero for  $\lambda \neq \lambda'$ , there may also be resonance with two distinct excitonic energies.

### 2.3 Field-Induced Second-Harmonic Generation

Among higher-order responses that can be extracted from Eq. (4), we look at the FI-SHG.

Let's consider a system with no second-harmonic response. In presence of an external field, the polarization in a given direction acquires contributions of the form,

$$P(2\omega^\pm) = \hat{\chi}^{(3)}(2\omega \pm \nu; \nu, \omega, \omega) E_1(\nu) E_2^2(\omega). \quad (7)$$

If  $E_1$  is static, i.e.  $\nu = 0$ , the third order susceptibility extracted from this contribution to the polarization gives the FI-SHG. Similarly, if  $\nu \ll \omega$ , i.e.  $E_1$  is in the THz range, we have  $2\omega \pm \nu \approx 2\omega$  and the expression in Eq. (7) can be rewritten as,

$$P(2\omega^\pm) \approx \hat{\chi}^{(3)}(2\omega; \nu, \omega, \omega) E_1(\nu) E_2^2(\omega). \quad (8)$$

Then, summing the  $\chi^{(3)}$  extracted by  $P(2\omega^+)$  and  $P(2\omega^-)$ , one obtains the corresponding FI-SHG for low-frequency time-dependent pump fields.

## 3 Signal processing: nonlinear susceptibilities

Adding an extra field to the formalism presented in Ref. [11] to obtain Eq. (1) is straightforward. The challenging part, and the main contribution of this work, is finding feasible, accurate strategies for extracting the relevant nonlinear susceptibilities from the resulting polarization  $\mathbf{P}(t)$ . A strategy based on the discrete-Fourier transform (DFT) is used in Ref. [11] (Sec. 3.1) for the case of one external monochromatic external field. This analysis can be extended to more external monochromatic fields (Sec. 3.2), but as the common period for two, or more, (commensurate) frequencies can be of several hundreds of fs, this implies very long and computationally costly simulations. We thus propose an alternative strategy based on the least square fit (LSF), which turns out to be as accurate as the DFT without requiring too long simulations.

### 3.1 One external monochromatic field

As described in Ref. [11], the harmonic generation is obtained by the simulation of a system under the effect of an external periodic electric field with frequency  $\omega_L$ ,  $\mathcal{E}(t) = \mathcal{E}_0 \sin(\omega_L t) \Theta(t)$ . A dephasing term is added to the Hamiltonian [11] so that for simulation times larger than the dephasing time  $1/\gamma_{\text{deph}}$ , the resulting time-dependent polarization can be written as<sup>1</sup>:

$$\mathbf{P}(t) = \sum_{n=-\infty}^{\infty} \mathbf{p}^{(n)} \exp[-i\omega^{(n)}t], \quad (9)$$

with  $\omega^{(n)} = n\omega_L$ . The complex Fourier components  $\mathbf{p}_n$  can be determined by truncating the Fourier series to an order  $S$  and sampling  $2S + 1$  values  $\mathbf{P}_i \equiv \mathbf{P}(t_i)$  within a period  $T_L = 2\pi/\omega_L$ . For each direction  $\alpha$ , this yields to

$$\sum_{n=-S}^S \mathcal{F}_i^{(n)} p_\alpha^{(n)} = P_{\alpha,i} \quad i = 1, 2S + 1, \quad (10)$$

where  $\mathcal{F}_i^{(n)} \equiv \exp[-i\omega^{(n)}t_i]$ . The solution of the  $(2S + 1)$  system of linear equations [Eq.(10)] outputs the  $p_\alpha^{(n)}$ , from which in turn one gets the  $n^{\text{th}}$ -order susceptibility by dividing by the  $n^{\text{th}}$  power of the  $\alpha$  component of  $\mathcal{E}_0$ . The nonlinear susceptibilities converge rapidly with  $S$ : in Ref. [11] it was found that second-order susceptibilities converge already with  $S = 4$  and third-order susceptibilities with  $S = 6$ .

### 3.2 Two external monochromatic fields

We consider two monochromatic fields, with commensurate frequencies,  $\omega_1$  and  $\omega_2$ . Frequencies are commensurate as long as they are rational numbers (that is  $\omega_1, \omega_2 \in \mathbf{Q}$ ), which is the case in numerical implementations. The greatest common divisor of  $\omega_1$  and  $\omega_2$  leads to the fundamental frequency,

$$\omega_0 = \frac{\text{gcd}(\lfloor 10^m \omega_1 \rfloor, \lfloor 10^m \omega_2 \rfloor)}{10^m}, \quad (11)$$

where  $m = \max(n_1, n_2)$  and  $n_1$  and  $n_2$  are the number of decimals in  $\omega_1$  and  $\omega_2$ , respectively.

The resulting polarization  $\mathbf{P}(t)$  is periodic with period  $T = 2\pi/\omega_0$  and hence can be written as a Fourier series as in Eq. (9), in terms of the harmonics of  $\omega_0$ . As the frequencies of the external fields, are multiple of the fundamental frequency,  $\omega_1 = M\omega_0$  and  $\omega_2 = N\omega_0$ , then the  $|M \pm N|$  harmonics correspond to the SFG/DFG. When it comes to setting up the system of linear equations Eq. (10), the sum over the harmonics must be truncated to an appropriate  $S$  to include these processes (that is  $S \gtrsim M + N$ ). When compared with a single external field, the dimension of system of linear equations is significantly larger. More critically,  $T$  can be very long for any pair of frequencies with more than one decimal (see Fig. 3). Depending on the ratio of  $\omega_1$  and  $\omega_2$ ,  $T$  can be orders of magnitude larger than the typical laser periods in the near-infrared to near-UV range ( $\approx 1 - 5$  fs). As the computational expense increases linearly with simulation time, using these approaches to process the polarization signal from two monochromatic fields, may lead to computationally intensive simulations.

<sup>1</sup>In general, the signal is sampled after a time which is about 6 times the dephasing time of the system. Then, the (spurious) term in the response functions arising from the sudden switch-on of the external field is negligible.

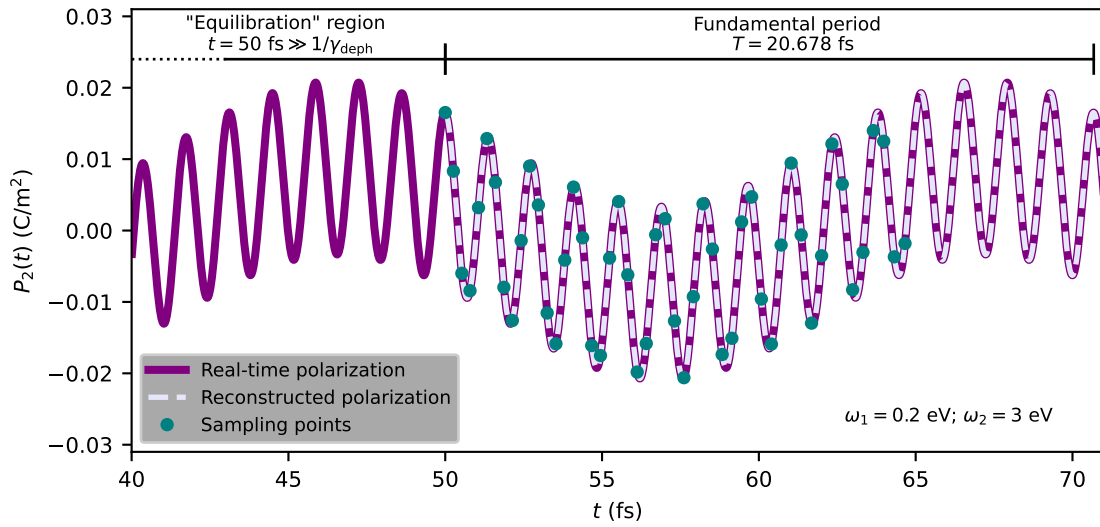


Figure 2: The time-dependent polarization (purple solid line) of  $h$ -BN calculated at the independent particle level with two electric fields ( $\omega_1 = 0.2 \text{ eV}$ ,  $\omega_2 = 3 \text{ eV}$ ). The signal can be divided into two regions: an initial “equilibration” region (up to  $t \gg \gamma_{\text{deph}}$ , here  $t = 50 \text{ fs}$ ) during which the system’s eigenfrequencies are suppressed by dephasing and a region where Eq. (12) holds. In the second region the polarization is logarithmic sampled (teal dots) within a converged time window of 15 fs, smaller than the fundamental period of 20.678 fs of the signal. This sampling time is sufficient to correctly determine the Fourier coefficients by the nonlinear least square fit (LSF) as verified by reconstructing the polarization (lavender dashed line) within the fundamental period using the Fourier coefficients and the truncated Eq. (12).

Alternatively, we can expand the polarization  $\mathbf{P}(t)$  as the product of two Fourier series, one in terms of the harmonics of  $\omega_1$  and the other in terms of the harmonics of  $\omega_2$ ,

$$\mathbf{P}(t) = \sum_{n,m=-\infty}^{\infty} \mathbf{C}^{(n,m)} \exp[-i(n\omega_1 + m\omega_2)t], \quad (12)$$

where the matrix of the Fourier coefficients is denoted as  $\mathbf{C}^{(n,m)}$ . The Fourier coefficients can be found by the solution of the system of  $(2S_1 + 1)(2S_2 + 1)$  linear equations

$$\sum_{n=-S_1}^{S_1} \sum_{m=-S_2}^{S_2} \mathcal{F}_i^{(n,m)} C_\alpha^{(n,m)} = P_{\alpha,i}, \quad (13)$$

where  $\mathcal{F}_i^{(n,m)} \equiv \exp[-i(n\omega_1 + m\omega_2)t_i]$  and  $S_1, S_2$  are the maximum number of harmonics considered for each external field. Compared to the DFT with one external field, it is straightforward to identify the relevant coefficients, for example,  $n = 1, m = 1$  gives the SFG and  $n = 2, m = \pm 1$  the FI-SHG (choosing  $\omega_2 = \Omega$ ). On the other hand, generally, the system of linear equations in Eq. (13) is ill-conditioned. To solve Eq. (13), we calculate the Moore-Penrose inverse [23, 24], also called pseudoinverse, of  $\mathcal{F}_i^{(n,m)}$  by using the singular value decomposition (SVD). This approach (that we will refer to as SVD) allows to work with a much smaller sampling time than  $T$ , so to significantly reduce the time from the simulations when compared with the DFT.

A further approach to obtain the Fourier coefficients is by solving a nonlinear least squares problem [25]. This consists in finding the set of  $C_\alpha^{(n,m)}$  that minimizes:

$$\sum_{i=1}^N |P_\alpha(t_i) - \bar{P}_\alpha(t_i)|^2, \quad (14)$$

where  $N$  is the number of sampling points and  $\bar{\mathbf{P}}$  is the Fourier series of Eq. (12) truncated to an order of  $S$ . Similarly to the SVD-based approach, the main advantage of the LSF over the DFT is that it is sufficient to sample part of the period  $T$  to find the Fourier coefficient accurately. For instance, for  $h$ -BN, Fig. 2 compares the polarization from the simulation with that reconstructed from Eq. (12) with the coefficients obtained from LSF. Although only 15 fs are sampled, the LSF provides an accurate result.

The accuracy and performance of the three approaches are contrasted in Fig. 3 for the SFG of  $h$ -BN. Using the approaches based on the SVD and the LSF allows to cut simulation time by a factor 26 compared to the DFT.

### 3.2.1 Further numerical considerations

For the LSF to be accurate, one must carefully sample the key features of the signal, e.g. minima, maxima and turning points. This implies that, in general, the LSF needs more sampling points  $P_i^\alpha$  (that is a higher sampling rate) than the DFT. This does not impact the cost of the simulations since a small time step is needed to integrate the equation of motion in Eq. (1). We found that non-uniform sampling (logarithmic or randomized) is more effective—thus reducing the sampling rate—than uniform sampling in capturing the key features of the signal, especially for high-frequency signals. An example of logarithmic sampling for LSF is shown in Fig. 3.

Another aspect to consider is which element of the susceptibility tensor to calculate. Depending on the crystal symmetry, certain tensor elements are equivalent; however, the directions in which the linear response is non-zero, tend to be less precise and more unstable. This is due to two factors. First, the spurious signal arising from the sudden

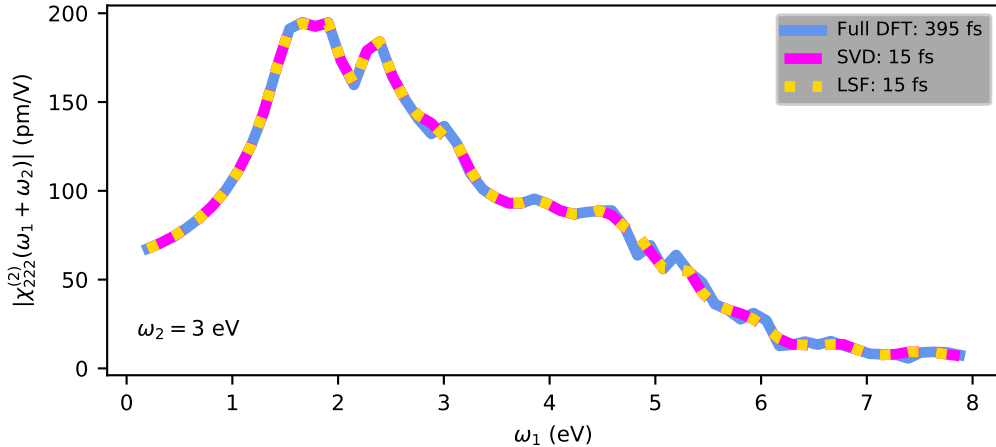


Figure 3: SFG of *h*-BN with a pump frequency  $\omega_2 = 3$  eV obtained at the IPA level using the full discrete Fourier transformation (DFT) (blue solid line), singular value decomposition (SVD) (magenta dashed line), and the nonlinear least square fit (LSF) (yellow dotted line). Results obtained with different sampling times are shown. The DFT needs a sampling time (395 fs) about 26 times larger than the SVD and LSF (15 fs).

switch-on is stronger. Second, the fitting procedure is less accurate since the linear response coefficient is about 6 orders of magnitude larger than the SHG, SFG and DFG ones. Therefore, if possible, one must choose the directions where the linear response is absent. For example, in the case of the second-order response for 2D hexagonal systems such as those studied here, it is more convenient to study the off-diagonal elements, e.g.,  $\chi_{122}^{(2)}$ , given that  $\chi_{122}^{(2)} = \chi_{222}^{(2)}$  by crystal symmetry.

Furthermore, a worst case for the LSF is when  $\omega_1 \approx \omega_2$ . When they are exactly equal, the least square problem is ill-posed. For example, if we write down the first term of the second-order polarization:

$$P^{(2)} = \chi^{(2)}(2\omega_1; \omega_1, \omega_1) \mathcal{E}^2(\omega_1) + \chi^{(2)}(2\omega_2; \omega_2, \omega_2) \mathcal{E}^2(\omega_2) + \chi^{(2)}(\omega_1 + \omega_2; \omega_1, \omega_2) \mathcal{E}(\omega_1) \mathcal{E}(\omega_2) + \dots$$

and  $\omega_1 \approx \omega_2$  SHG and SFG become equivalent, their coefficients cannot be fixed using least square optimization. Similar issues arise if one of the frequency is an integer multiple of the other. In those cases, a few strategies may be adopted. One can eliminate the repeated terms in the fitting function, or use as starting values for the optimization those of the closest frequency already calculated, or simply interpolate the result from the neighbouring frequencies.

Note that the quasi-degenerate case is also the worst case for the DFT since closely spaced frequencies result in rapid beats in the signal. To accurately capture these beats, a very long sampling range is necessary to resolve the beat frequency ( $\omega_1 - \omega_2$ ). Ultimately, cases involving degenerate or quasi-degenerate frequencies are of little theoretical and experimental interest. Theoretically, for degenerate frequencies, the procedures in Ref. [11] (see Sec. 3.1) can extract the second-harmonic, while experimentally the interest lies in distinct frequencies resonant with different electron-hole excitations [8].

System	$\mathbf{k}$ -points	$N_b$	$\epsilon_{\text{cut}}$ (Ha)	$\epsilon_{\text{bands}}$	$\Delta E_{\text{so}}$ (eV)	$L_z$ (Å)	$d_{\text{eff}}$ (Å)
MoS <sub>2</sub>	30 × 30 (21 × 21)	4-13	5	200	0.72	10.88	6.15
<i>h</i> -BN	30 × 30 (18 × 18)	3-7	5	200	3.35	10.58	3.33
2L- <i>h</i> -BN	30 × 30 (18 × 18)	5-14	-	-	-	10.58	6.66

Table 1: All the parameters used in the nonlinear response calculations for both MoS<sub>2</sub> and *h*-BN monolayers: the  $\mathbf{k}$ -point sampling used in the IPA (TD-aGW in parentheses), the range of bands considered, the cut-off,  $\epsilon_{\text{cut}}$ , and the number of bands,  $\epsilon_{\text{bands}}$ , used to converge the dielectric function  $\epsilon_{\mathbf{G},\mathbf{G}'}$ , the value of shift ( $\Delta E_{\text{so}}$ ) for the scissor operator applied to the Kohn-Sham band structure, the height of the supercell,  $L_z$  and the effective layer thickness,  $d_{\text{eff}}$ . For the 2L-*h*-BN calculations are only at IPA level, so no information about dielectric constant and scissor operator are reported.

## 4 Computational Details

Ground-state properties of the *h*-BN mono- and bilayer and of MoS<sub>2</sub> monolayer are calculated within the density functional theory using the Quantum-Espresso code [26]. We employ the Perdew-Burke-Ernzerhof (PBE) functional [27] with scalar-relativistic optimized norm-conserving pseudopotentials from the PseudoDojo repository (v0.4) [28] for the *h*-BN and FHI [29] for MoS<sub>2</sub>. The Kohn-Sham Hamiltonian is diagonalized for a given number of states (see  $\mathbf{k}$ -points and bands  $N_b$  in Table 1). These states are used as basis set to represent all operators that enter in the Eq. (1). All real-time simulations are carried out using the Yambo code [30]. The EOMs [Eq. (1)] are propagated using the Crank-Nicolson integrator with a time-step of 0.01 fs. In order to take dephasing into account, sampling was taken between 50-200 fs in all simulations. The static dielectric function  $\epsilon_{\mathbf{G},\mathbf{G}'}$  that enters in the calculation of screened-exchange self-energy,  $\Sigma_{\text{SEX}}$  in Eq. (2), is calculated within the random-phase approximation (see Ref. [30] for more details). All calculations are performed in a supercell, so for each system, the susceptibility extracted from the time-dependent polarization is rescaled to the effective thickness,  $d_{\text{eff}}$ , resulting in  $\chi_{\text{rescaled}}(\omega) = L_z/d_{\text{eff}} \cdot \chi(\omega)$  where  $L_z$  labels the  $z$  dimension of the supercell. To get the SFG and DFG spectra, we carry out simulations for all frequency couples,  $\omega_i, \omega_j$  in Eq. 3.2, in the desired energy ranges. We use the YamboPy code [31] to extract the relevant susceptibilities from the resulting polarizations [Eq. (4)], as detailed in Sec. 3. All parameters that enter in the different parts of the simulations are reported in Table 1.

## 5 Results

We apply the approach outlined in Secs. 2-3 to the SFG and DFG in *h*-BN and MoS<sub>2</sub> monolayers (Secs. 5.1-5.2). *h*-BN monolayer is a wide band gap insulator with strong excitonic features and provides a clear example of the need for an accurate inclusion of excitonic effects. MoS<sub>2</sub> monolayer is one of the most widely studied 2D material, including its SFG/DFG [4, 7]. For SFG and DFG, we show results in a heatmap, in which each point has been obtained by a separate real-time simulation. As a guide to reading such heatmaps (see e.g. Fig. 4), we can refer to Eqs. (5)-(6). The susceptibilities corresponding to SFG/DFG have poles both at one-photon ( $\omega_{1,2} = \Omega_\lambda$ ) and at two-photon ( $\omega_1 \pm \omega_2 = \Omega_\lambda$ ) resonances with single-particle transitions (or with excitons) in the system. The one-photon resonances correspond to vertical ( $\omega_1$ ) and horizontal ( $\omega_2$ ) lines in the SFG and DFG heatmaps. In the SFG heatmap, the two-photon resonances correspond to negative slope lines running from  $\omega_2 = \Omega_\lambda$  to  $\omega_1 = \Omega_\lambda$ , while in DFG they correspond to positive

slope lines starting at  $\omega_2 = \Omega_\lambda$  and  $\omega_1 = \Omega_\lambda$ . Further, the diagonal  $\omega_1 = \omega_2$  corresponds to the SHG in the SFG and the optical rectification in the DFG heatmap. In Sec. 5.3, we consider THz-induced second-harmonic generation in 2L-*h*-BN. This system has inversion symmetry and thus has zero SHG at zero-field.

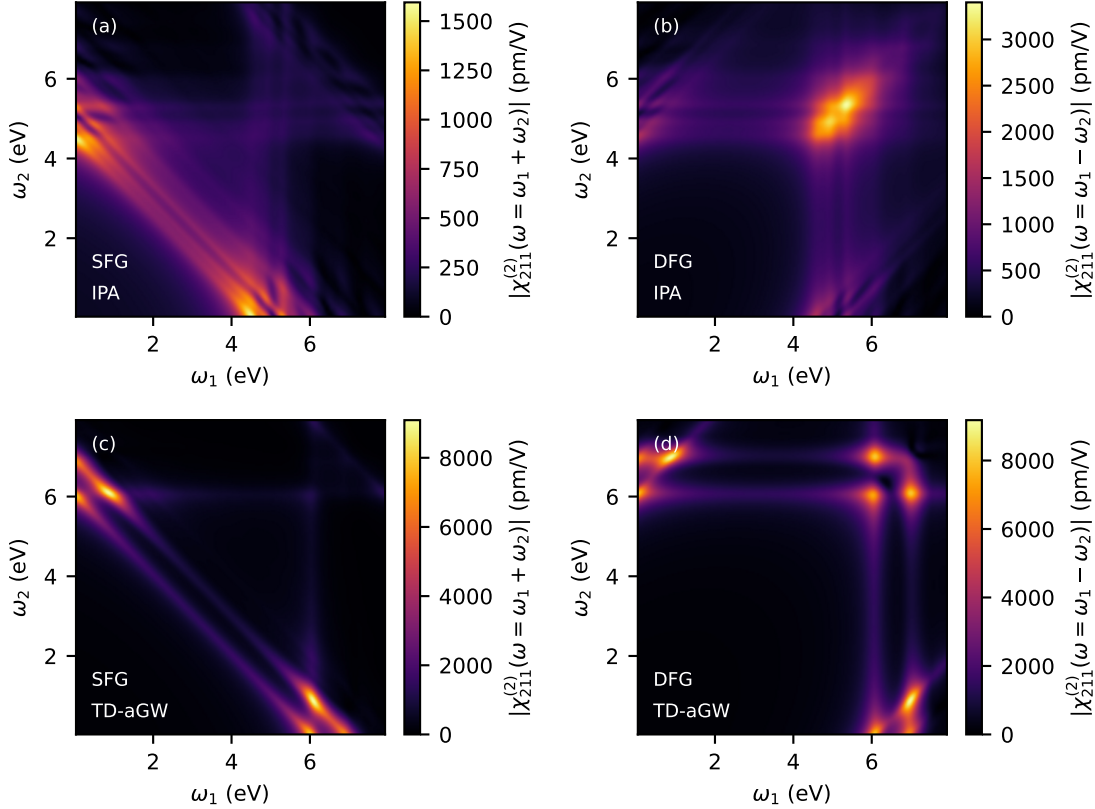


Figure 4: SFG/DFG spectra for *h*-BN in panels (a), (b) at the independent particle level and in panels (c), (d) at the TD-aGW level. These heatmaps have been generated using a frequency grid of  $\omega_1 \times \omega_2 = 96 \times 96$  points. For each frequency pair a real-time simulation was run and the output signal processed.

### 5.1 SFG and DFG in monolayer *h*-BN

In Fig. 4 we report the SFG and DFG spectra for *h*-BN both at the IPA and TD-aGW approximation level. For SFG, the line  $\omega_1 = \omega_2$  corresponds to the SHG, already calculated in Ref. [13]. In Fig. 4, we report the SFG and DFG spectra for *h*-BN both at the IPA and TD-aGW level. At the IPA level, the SFG spectrum (panel (a)) of *h*-BN is dominated by two-photon resonances with single-particle transitions between 4-6 eV (negative slopes bands). In particular, the lowest-energy band corresponds to the transition from the valence band minimum to the conduction band maximum. The one-photon transitions (vertical and horizontal bands) are much weaker though a significant enhancement is observed for part of the spectra both resonant with one- and two-photon. In particular, this portion of the SFG spectrum is twice as intense as the SHG (the  $\omega_1 = \omega_2$  diagonal). The DFG spectrum (panel (b)) is dominated by the resonant optical rectification between 4-6 eV ( $\omega_1 = \omega_2$ ). Further, one-photon resonances (vertical and horizontal bands) are visible, again enhanced when two-photon resonances are also present. These results can be straightforwardly related to the IPA absorption spectrum (see e.g. [13]), which presents

a broad peak between 4-6 eV).

As expected, the addition of the electron-hole interaction drastically changes the SFG/DFG spectra<sup>2</sup>. Sharper and much stronger (note the different color scale) features appear in the TD-aGW spectra, corresponding to the  $E_1, E_2$  excitonic peaks at around 6.1 eV and 7 eV. [32]. Two-photon resonances with the two excitons are clearly visible in the SFG spectrum (negative slope lines in panel (c)) and DFG spectrum (positive slope lines starting at the exciton energy in panel (d)). One-photon resonances are also visible (as vertical/horizontal lines). The responses are significantly enhanced in the SFG (DFG) when one laser is resonant with  $E_1$  ( $E_2$ ) and the second laser with  $E_2 - E_1$ . These spectral features correspond to the first and third terms in Eq. (6) and provide a measure of the strength of exciton-exciton transitions. In the DFG spectrum, strong features are visible as well on the diagonal, corresponding to the exciton-resonant optical rectification and when one laser is resonant with one exciton and the second with the other (corresponding to the second and fourth term in Eq. (6)).

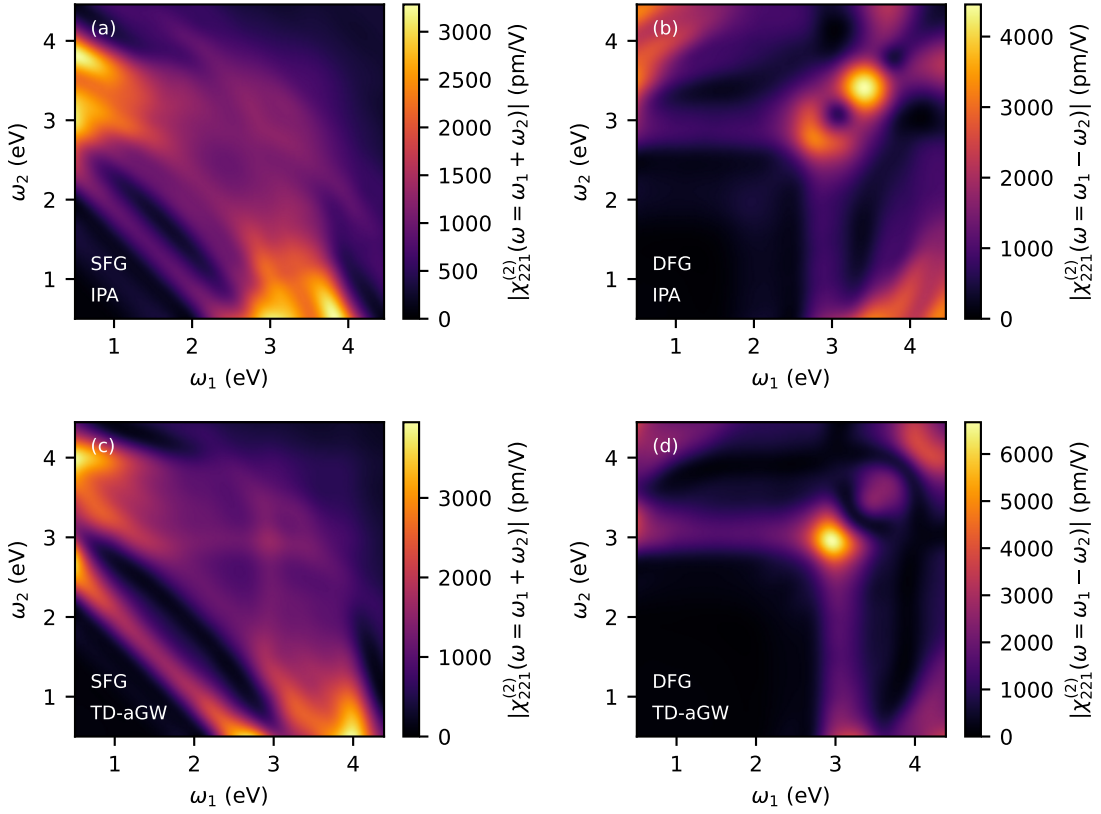


Figure 5: SFG/DFG spectra for MoS<sub>2</sub> in panels (a) and (b) at the independent particle level and in panel (c), (d) at the TD-aGW level. These heatmaps have been generated using a frequency grid of  $\omega_1 \times \omega_2 = 96 \times 96$  points for the IPA and  $\omega_1 \times \omega_2 = 72 \times 72$  for the TD-aGW. For each frequency pair a real-time simulation was run and the output signal processed. .

<sup>2</sup>Note that the shift of the onset is due to the addition of the scissor operator in Table 1 partially compensated by the exciton binding energy.

## 5.2 SFG and DFG in monolayer MoS<sub>2</sub>

In Fig. 5, we report the SFG and DFG spectra for the monolayer MoS<sub>2</sub> at the IPA and TD-aGW level. When compared with *h*-BN, the differences between the IPA and TD-aGW spectra are less striking, as already observed for the absorption [33] and the SHG [13]. Similarly to what observed for the SHG [13, 34, 35], a significant enhancement is seen at resonances with the C exciton ( $\approx 3$  eV), while the weaker the A and B excitons ( $\approx 2.2$  eV, as spin-orbit coupling is not included the peaks are degenerate) show minimal excitonic enhancement. The SFG spectrum shows a strong two-photon resonance with the C exciton (negative slope line) while the DFG spectrum shows a strong one-photon resonance (vertical/horizontal line) and a strong exciton resonant optical rectification. Though less evident than for *h*-BN, there is an enhancement in the intensity in correspondence of exciton-exciton transitions. In the SFG (panel (c)), the signal is enhanced when one laser is resonant with the A/B exciton (about 2.2 eV) while the frequency of the second matches the energy difference between the C and A/B excitons. In the DFG (panel (d)), the signal is enhanced when one laser is resonant with the C exciton (about 3 eV) while the frequency of the second corresponds to the energy difference between the C and A/B excitons. Simulations results align with existing measurements. SFG has been observed [36] at 2.9 eV when laser fields at 1.2 eV and 1.9 eV were injected. The DFG has been observed [7] fixing one laser at 3.06 eV and varying the second between 0.79 and 0.95 eV showing an enhancement of the signal between 2.1-2.2 eV that the authors attributed to excitonic effects in this region.

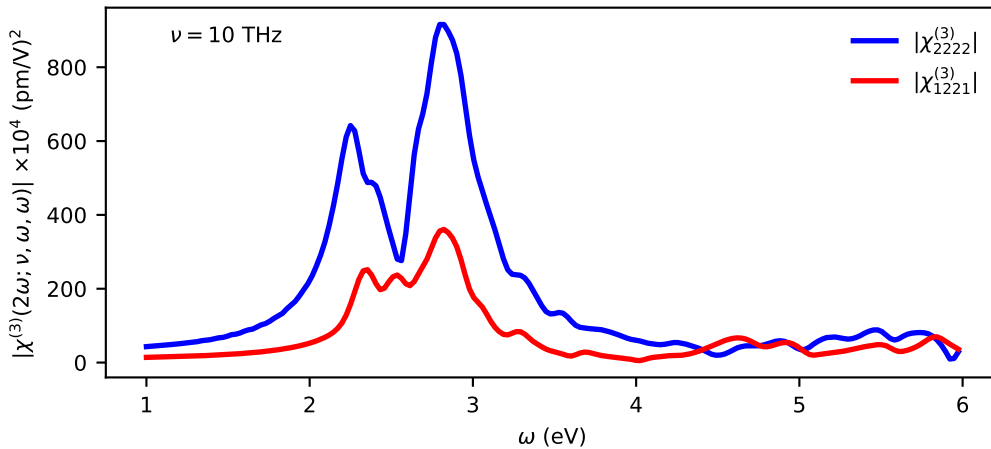


Figure 6: Calculated THz field-induced second-harmonic generation of bilayer *h*-BN with  $\nu=10$  THz at the IPA level. Each curve consists of 192 frequency steps between  $\omega = 1 - 6$  eV.

## 5.3 Field-Induced Second-Harmonic Generation

In Fig. 6 we report the third order susceptibility corresponding to the FI-SHG in bilayer *h*-BN. For each frequency  $\omega$ , we run a real-time simulation in presence of the THz pump ( $\nu = 10$  THz). The response functions reported in the figure correspond to two possible experimental configurations, a pump and probe in *y* direction ( $\chi_{2222}^{(3)}$ ), and pump in *x* and probe in *y* direction ( $\chi_{1221}^{(3)}$ ). In both configurations, the susceptibility shows a strong resonance at half of the gap, around 2-3 eV, similar to the standard SHG in monolayer *h*-BN [13]. We found that the intensity of the response when pump and probe are parallel

is higher than the perpendicular configuration. The order of magnitude of the  $\chi^{(3)}$  is comparable with that of bulk ferroelectric oxides which are known for their excellent nonlinear properties [37]. This result implies that two-dimensional crystals can be used as a detector for THz radiation [38].

## 6 Conclusions

In this work, we present a computational framework to study sum/difference frequency generation by means of real-time simulations in presence of multiple laser fields. With multiple fields, the challenge is the signal processing required to extract the nonlinear susceptibilities. In particular, using a discrete Fourier transform approach may require very long and thus computationally costly simulations. We found that approaches based either on the singular value decomposition and the least squares optimization give accurate results with short sampling time and allow to reduce significantly the simulation time. These approaches enable the calculation of second-order response functions, as SFG/DFG, and higher nonlinear response functions, as FI-SHG, including excitonic effects within many-body theory. For the system studied, monolayer *h*-BN and MoS<sub>2</sub>, we showed that including excitonic effects in SFG/DFG spectra is critical. In both materials, we predict strong features corresponding to exciton transitions, as recently experimentally observed for another layered material [8]. Further, the results on FI-SHG for bilayer demonstrate that the approach can be used to predict and interpret nonlinear terahertz spectroscopy of solids [39]. Finally, the approach presented can be coupled to atomic vibrations by using finite displacement methods [40,41] opening the way to simulate other spectroscopic techniques such as Coherent Anti-Stokes Raman spectroscopy (CARS). The latter is a powerful nonlinear optical technique for probing vibrational modes in molecular and solid-state structures. CARS involves two laser beams exciting a vibrational state, and a third beam generating a coherent Anti-Stokes signal, allowing for high resolution imaging [42]. CARS can be seen as a combination of SFG and DFG processes, and therefore the method shown in this study could be employed to study the nonresonant CARS response. Since the pure nonresonant CARS is not directly available experimentally [43], the *ab initio* real-time simulation is a promising feature to support CARS measurements.

## Acknowledgments

The authors gratefully acknowledge financial support from the Deutsche Forschungsgemeinschaft (DFG) through the research group FOR5044 (ID: 426703838; <http://www.For5044.de>). Calculations for this research were conducted on the Lichtenberg high-performance computer of the TU Darmstadt and at the Höchstleistungsrechenzentrum Stuttgart (HLRS). The authors furthermore acknowledge the computational resources provided by the HPC Core Facility and the HRZ of the Justus-Liebig-Universität Gießen. C.A. acknowledges B. Demoulin and A. Saul for the management of the computer cluster *Rosa*. C.A. acknowledges the COLIBRI No. ANR-22-CE30-0027 ANR project. C.A. and M.G. acknowledge funding from European Research Council MSCA-ITN TIMES under grant agreement 101118915 and from AMUtech. M.G. acknowledges funding from the UKRI Horizon Europe Guarantee funding scheme (EP/Y032659/1).

## References

- [1] K. Niu and R. A. Marcus, *Sum frequency generation, calculation of absolute intensities, comparison with experiments, and two-field relaxation-based derivation*, Proceedings of the National Academy of Sciences **117**(6), 2805 (2020), doi:10.1073/pnas.1906243117.
- [2] A. Morita, *Theory of sum frequency generation spectroscopy*, vol. 97, Springer, doi:doi.org/10.1007/978-981-13-1607-4 (2018).
- [3] J. A. Maytorena, W. L. Mochán and B. S. Mendoza, *Hydrodynamic model for sum and difference frequency generation at metal surfaces*, Physical review B **57**(4), 2580 (1998), doi:10.1103/PhysRevB.57.2580.
- [4] D. Li, W. Xiong, L. Jiang, Z. Xiao, H. Rabiee Golgir, M. Wang, X. Huang, Y. Zhou, Z. Lin, J. Song *et al.*, *Multimodal nonlinear optical imaging of MoS<sub>2</sub> and MoS<sub>2</sub>-based van der waals heterostructures*, ACS nano **10**(3), 3766 (2016), doi:10.1021/acsnano.6b00371.
- [5] T. Yang, E. Pollmann, S. Sleziona, E. Hasselbrink, P. Kratzer, M. Schleberger, R. K. Campen and Y. Tong, *Interaction between a gold substrate and monolayer MoS<sub>2</sub>: An azimuthal-dependent sum frequency generation study*, Phys. Rev. B **107**, 155433 (2023), doi:10.1103/PhysRevB.107.155433.
- [6] K. Yao, E. Yanev, H.-J. Chuang, M. R. Rosenberger, X. Xu, T. Darlington, K. M. McCreary, A. T. Hanbicki, K. Watanabe, T. Taniguchi *et al.*, *Continuous wave sum frequency generation and imaging of monolayer and heterobilayer two-dimensional semiconductors*, ACS nano **14**(1), 708 (2019), doi:10.1021/acsnano.9b07555.
- [7] Y. Wang, M. Ghotbi, S. Das, Y. Dai, S. Li, X. Hu, X. Gan, J. Zhao and Z. Sun, *Difference frequency generation in monolayer MoS<sub>2</sub>*, Nanoscale **12**(38), 19638 (2020), doi:10.1039/D0NR01994A.
- [8] Y. Kim, H. Kim, H. Jang, J.-H. Ahn and J. Lee, *Dual resonant sum frequency generations from two-dimensional materials*, Nano letters **20**(6), 4530 (2020), doi:10.1021/acs.nanolett.0c01363.
- [9] D. Sangalli, M. D'Alessandro and C. Attaccalite, *Exciton-exciton transitions involving strongly bound excitons: An ab initio approach*, Phys. Rev. B **107**, 205203 (2023), doi:10.1103/PhysRevB.107.205203.
- [10] V. A. Margulis, E. E. Muryumin and E. A. Gaiduk, *Spectral characteristics of the sum-frequency generation from atomically thin hexagonal crystals lacking center-of-inversion symmetry*, Journal of Optics **17**(6), 065502 (2015), doi:10.1088/2040-8978/17/6/065502.
- [11] C. Attaccalite and M. Grüning, *Nonlinear optics from an ab initio approach by means of the dynamical Berry phase: Application to second-and third-harmonic generation in semiconductors*, Phys. Rev. B **88**(23), 235113 (2013), doi:10.1103/PhysRevB.88.235113.
- [12] I. Souza, J. Íñiguez and D. Vanderbilt, *Dynamics of Berry-phase polarization in time-dependent electric fields*, Phys. Rev. B **69**, 085106 (2004), doi:10.1103/PhysRevB.69.085106.

- [13] M. Grüning and C. Attaccalite, *Second harmonic generation in h-bn and mos<sub>2</sub> monolayers: Role of electron-hole interaction*, Phys. Rev. B **89**, 081102 (2014), doi:10.1103/PhysRevB.89.081102.
- [14] M. Reid, I. V. Cravetchi and R. Fedosejevs, *Terahertz radiation and second-harmonic generation from inas: Bulk versus surface electric-field-induced contributions*, Phys. Rev. B **72**, 035201 (2005), doi:10.1103/PhysRevB.72.035201.
- [15] Y. Ding, Y. Zeng, X. Yu, Z. Liu, J. Qian, Y. Li, Y. Peng, L. Song, Y. Tian, Y. Leng *et al.*, *Terahertz-assisted even harmonics generation in silicon*, Iscience **25**(2) (2022), doi:10.1016/j.isci.2022.103750.
- [16] S. Grillo, E. Cannuccia, M. Palummo, O. Pulci and C. Attaccalite, *Tunable second harmonic generation in 2D materials: Comparison of different strategies*, SciPost Phys. Core **7**, 081 (2024), doi:10.21468/SciPostPhysCore.7.4.081.
- [17] C. Attaccalite, M. Grüning and A. Marini, *Real-time approach to the optical properties of solids and nanostructures: Time-dependent bethe-salpeter equation*, Physical Review B **84**(24), 245110 (2011), doi:10.1103/PhysRevB.84.245110.
- [18] W. Kohn and L. J. Sham, *Self-consistent equations including exchange and correlation effects*, Physical review **140**(4A), A1133 (1965), doi:10.1103/PhysRev.140.A1133.
- [19] G. Strinati, *Application of the Green's functions method to the study of the optical properties of semiconductors*, Nuovo Cimento Rivista Serie **11**, 1 (1988), doi:10.1007/BF02725962.
- [20] R. W. Boyd, A. L. Gaeta and E. Giese, *Nonlinear optics*, In *Springer Handbook of Atomic, Molecular, and Optical Physics*, pp. 1097–1110. Springer, doi:10.1007/978-3-030-73893-8\_76 (2008).
- [21] A. Riefer and W. Schmidt, *Solving the bethe-salpeter equation for the second-harmonic generation in Zn chalcogenides*, Physical Review B **96**(23), 235206 (2017), doi:10.1103/PhysRevB.96.235206.
- [22] R. Leitsmann, W. Schmidt, P. Hahn and F. Bechstedt, *Second-harmonic polarizability including electron-hole attraction from band-structure theory*, Physical Review B—Condensed Matter and Materials Physics **71**(19), 195209 (2005), doi:10.1103/PhysRevB.71.195209.
- [23] E. H. Moore, *On the reciprocal of the general algebraic matrix*, Bulletin of the american mathematical society **26**, 294 (1920), <https://cir.nii.ac.jp/crid/1573387450082342272>.
- [24] R. Penrose, *A generalized inverse for matrices*, Mathematical Proceedings of the Cambridge Philosophical Society **51**(3), 406–413 (1955), doi:10.1017/S0305004100030401.
- [25] P. Virtanen, R. Gommers, T. E. Oliphant, M. Haberland, T. Reddy, D. Cournapeau, E. Burovski, P. Peterson, W. Weckesser, J. Bright, S. J. van der Walt, M. Brett *et al.*, *SciPy 1.0: Fundamental Algorithms for Scientific Computing in Python*, Nature Methods **17**, 261 (2020), doi:10.1038/s41592-019-0686-2.
- [26] P. Giannozzi *et al.*, *Quantum espresso: a modular and open-source software project for quantum simulations of materials*, J. Phys. Condens. Matter **21**, 395502 (2009), <http://www.quantum-espresso.org>.

- [27] J. P. Perdew, K. Burke and M. Ernzerhof, *Generalized gradient approximation made simple*, Phys. Rev. Lett. **77**, 3865 (1996), doi:10.1103/PhysRevLett.77.3865.
- [28] M. van Setten, M. Giantomassi, E. Bousquet, M. Verstraete, D. Hamann, X. Gonze and G.-M. Rignanese, *The PseudoDojo: Training and grading a 85 element optimized norm-conserving pseudopotential table*, Computer Physics Communications **226**, 39 (2018), doi:https://doi.org/10.1016/j.cpc.2018.01.012, <http://www.pseudo-dojo.org/>.
- [29] P. Rivero, V. Manuel García-Suárez, D. Pereñiguez, K. Utt, Y. Yang, L. Bellaiche, K. Park, J. Ferrer and S. Barraza-Lopez, *Systematic pseudopotentials from reference eigenvalue sets for DFT calculations: Pseudopotential files*, Data in Brief **3**, 21 (2015), doi:https://doi.org/10.1016/j.dib.2014.12.005.
- [30] D. Sangalli, A. Ferretti, H. Miranda, C. Attaccalite, I. Marri, E. Cannuccia, P. Melo, M. Marsili, F. Paleari, A. Marrazzo, G. Prandini, P. Bonfà *et al.*, *Many-body perturbation theory calculations using the Yambo code*, Journal of Physics: Condensed Matter **31**(32), 325902 (2019), <https://www.yambo-code.eu/>.
- [31] H. P. C. Miranda, F. Paleari, A. Molina-Sanchez and J. Castelo, *YamboPy: a pre/post-processing, data analysis and plotting tool for Yambo and Quantum Espresso*, <https://github.com/yambo-code/yambopy> (2024).
- [32] L. Wirtz, A. Marini and A. Rubio, *Excitons in boron nitride nanotubes: dimensionality effects*, Physical review letters **96**(12), 126104 (2006), doi:10.1103/PhysRevLett.96.126104.
- [33] A. Molina-Sánchez, D. Sangalli, K. Hummer, A. Marini and L. Wirtz, *Effect of spin-orbit interaction on the optical spectra of single-layer, double-layer, and bulk mos<sub>2</sub>*, Phys. Rev. B **88**, 045412 (2013), doi:10.1103/PhysRevB.88.045412.
- [34] J. Ruan, Y.-H. Chan and S. G. Louie, *Exciton enhanced nonlinear optical responses in monolayer h-BN and MoS<sub>2</sub>: Insight from first-principles exciton-state coupling formalism and calculations*, Nano Letters **0**(0), null (0), doi:10.1021/acs.nanolett.4c03434.
- [35] K. Beach, M. C. Lucking and H. Terrones, *Strain dependence of second harmonic generation in transition metal dichalcogenide monolayers and the fine structure of the c exciton*, Phys. Rev. B **101**, 155431 (2020), doi:10.1103/PhysRevB.101.155431.
- [36] H. Jang, K. P. Dhakal, K.-I. Joo, W. S. Yun, S. M. Shinde, X. Chen, S. M. Jeong, S. W. Lee, Z. Lee, J. Lee, J.-H. Ahn and H. Kim, *Transient shg imaging on ultrafast carrier dynamics of mos<sub>2</sub> nanosheets*, Advanced Materials **30**(14), 1705190 (2018), doi:https://doi.org/10.1002/adma.201705190, <https://advanced.onlinelibrary.wiley.com/doi/pdf/10.1002/adma.201705190>.
- [37] C. Dues, M. J. Müller, S. Chatterjee, C. Attaccalite and S. Sanna, *Non-linear optical response of ferroelectric oxides: First-principles calculations within the time and frequency domains*, Phys. Rev. Mater. **6**, 065202 (2022), doi:10.1103/PhysRevMaterials.6.065202.
- [38] J. Chen, P. Han and X.-C. Zhang, *Terahertz-field-induced second-harmonic generation in a beta barium borate crystal and its application in terahertz detection*, Applied Physics Letters **95**(1) (2009), doi:10.1063/1.3176439.

- [39] T. Elsaesser, K. Reimann and M. Woerner, *Nonlinear terahertz spectroscopy of solids*, In *Concepts and Applications of Nonlinear Terahertz Spectroscopy, Second Edition*, 2053-2563, pp. 5–1 to 5–54. IOP Publishing, ISBN 978-0-7503-6492-8, doi:10.1088/978-0-7503-6492-8ch5 (2024).
- [40] Y. Gillet, M. Giantomassi and X. Gonze, *First-principles study of excitonic effects in raman intensities*, Phys. Rev. B **88**, 094305 (2013), doi:10.1103/PhysRevB.88.094305.
- [41] H. P. Miranda, S. Reichardt, G. Froehlicher, A. Molina-Sánchez, S. Berciaud and L. Wirtz, *Quantum interference effects in resonant raman spectroscopy of single- and triple-layer MoTe<sub>2</sub> from first-principles*, Nano Letters **17**(4), 2381 (2017), doi:10.1021/acs.nanolett.6b05345.
- [42] H. Lotem, R. T. Lynch and N. Bloembergen, *Interference between raman resonances in four-wave difference mixing*, Phys. Rev. A **14**, 1748 (1976), doi:10.1103/PhysRevA.14.1748.
- [43] F. Hempel, S. Reitzig, M. Rüsing and L. M. Eng, *Broadband coherent anti-Stokes Raman scattering for crystalline materials*, Physical Review B **104**(22), 224308 (2021), doi:10.1103/PhysRevB.104.224308.